EARTHQUAKE ENGINEERING AND STRUCTURAL DYNAMICS
Earthquake Engng Struct. Dyn. 2006; **35**:159–175
Published online 26 July 2005 in Wiley InterScience (www.interscience.wiley.com). DOI: 10.1002/eqe.512

Cyclic tests of post-tensioned precast CFT segmental bridge columns with unbonded strands

Chung-Che Chou*,†,‡ and Yu-Chih Chen§

Department of Civil Engineering, National Chiao Tung University, 1001 Ta-hsueh Rd., Hsinchu 300, Taiwan

SUMMARY

Two ungrouted post-tensioned, precast concrete-filled tube (CFT) segmental bridge columns were tested under lateral cyclic loading to evaluate the seismic performance of the column details. The specimens included a load stub, four equal-height circular CFT segments, and a footing. Strands were placed through the column and post-tensioned to provide a precompression of the column against the footing. One specimen also contained energy-dissipating devices at the base to increase the hysteretic energy. The test results showed that (1) both specimens could develop the maximum flexural strength at the design drift and achieve 6% drift with small strength degradation and residual displacement, (2) the proposed energy-dissipating device could increase energy dissipation in the hysteresis loops, and (3) the CFT segmental columns rotated not only about the base but also about the interface above the bottom segment. This study proposed and verified a method to estimate the experimental flexural displacement using two plastic hinges in the segmental column. Copyright © 2005 John Wiley & Sons, Ltd.

KEY WORDS: precast CFT segmental bridge column; unbonded strand; two plastic hinges

INTRODUCTION

Many studies [1–4] are available on the cyclic response of a concrete-filled tube (CFT) column, which consists of a steel tube filled with concrete. The tube not only raises the compression strength and ultimate strain of confined concrete but also provides the column's flexural strength. A bulge forms at the compression face of the plastic hinge region near the column base after the steel reaches yield strain, and increases with the load or drift until

*Correspondence to: Chung-Che Chou, Department of Civil Engineering, National Chiao Tung University, 1001 Ta-hsueh Rd., Hsinchu 300, Taiwan.
†E-mail: chchou@mail.nctu.edu.tw
‡Assistant Professor.
§Graduate Student Researcher.

Contract/grant sponsor: Continental Engineering Corporation
Contract/grant sponsor: Dywidag Systems International

Received 16 December 2004
Revised 28 March 2005
Accepted 20 May 2005

tensile fracture of the tube occurs. Both energy dissipation and ductility are increased because of the confinement from the steel tube, but loading the column to high drift produces large residual deformation.

To decrease the residual displacement of the column and avoid cast-in-place concrete construction, the application of precast segmental technology to the column may be a possible solution [5]. Hews and Priestley [6] investigated the cyclic behaviour of four unbonded precast concrete segmental columns under different aspect ratios, initial post-tensioning forces, and tube thicknesses. The bottom segment was encased in a steel tube and the upper segments were reinforced with standard spiral reinforcement. All specimens behaved in a ductile manner with low residual displacement, but severe spalling of concrete directly above the bottom segment except in the base was unexpected. The test results showed that the columns rotated about the base and the top interface of the bottom segment, but did not clarify the flexural displacement of the column due to rotations at the two locations.

OBJECTIVE

The goals of this study were: (1) to investigate experimentally the behaviour of two ungrouted post-tensioned, precast CFT segmental bridge columns under lateral cyclic loading, (2) to examine whether the hysteretic energy dissipation of the column increased with the proposed device equipped at the base, and (3) to develop a method for estimating the experimental, flexural displacement of the segmental column caused by rotations at the base and the interface above the bottom segment, respectively.

CFT SEGMENTAL COLUMN SPECIMEN DESIGN

Two full-scale post-tensioned CFT segmental bridge columns with a height of 14.7 m, a diameter of 3 m, and a supported dead weight of 22 MN (equal to $0.1 f_c' A_c$) were designed using the displacement-based approach [7]. The 28-day concrete strength, f_c', was specified as 35 MPa; the parameter A_c was the total concrete area. The column with an assumed effective damping value of 10% [6], of which half was assumed for hysteretic and elastic, was designed for 3.5% drift. The design ground acceleration based on soil type C [8] was specified as 0.7 g. To conduct a cyclic test of the column in the laboratory, the specimen was one-sixth of the prototype, with a corresponding design lateral force and moment, M_d, at the base of 194 kN and 475 kN-m [9], respectively.

Based on the research of Hewes and Priestley [6], the lateral force–lateral displacement relationship of a post-tensioned concrete segmental column exhibited a negative post-elastic stiffness in an early stage when the maximum axial force in the column exceeded $0.4 f_c' A_c$. With this axial load ratio, limited in the column to avoid such behaviour, and the maximum strand force, conservatively limited to $0.5 f_{pu} A_{st}$, the area of the strands, A_{st}, was calculated as follows:

$$A_{st} = \frac{0.4 f_c' A_c}{0.5 f_{pu}} = 2685 \text{ mm}^2 \quad (1)$$

where $f_{pu}(= 1860\,\text{MPa})$ is the ultimate tensile strength of the strand. Nineteen 15-mm diameter seven wire, uncoated, low-relaxation ASTM A416 Grade 270 strands were placed at the mid-depth of the cross-section.

The bottom segment was encased in an A36 steel tube with a wall thickness of 5 mm, which violates AISC's [10] required minimum thickness. The thickness in this study was specified to limit the extreme fibre concrete compression strain, as calculated using the confined concrete model [11], to less than $0.5\varepsilon_{cu}$ at the design drift and to the ultimate strain, ε_{cu}, at 6% drift. The other segments were encased in a 3-mm thick A36 steel tube. The steel tube did not extend to the full height of the segment, but terminated 25 mm above the face of the concrete to prevent contact between the steel tubes or between the bottom tube and a footing when the column was subjected to lateral loading. No segment used any transverse or longitudinal reinforcement. With the required lateral force at the design drift, the strand area from Equation (1), and the strain limits, the initial post-tensioning force calculated based on an iterative sectional analysis [6] was 2494 kN, equivalent to 44% of the ultimate strand strength.

The bottom segment height was specified to minimize the gap opening at the top interface of the bottom segment in combined axial and flexural loadings. The moment distribution along the column height for the design drift is shown in Figure 1, where $M_{2,1}$ and $M_{2,2}$ are the moment capacities when the neutral axis position is located at the extreme fibre and cross-section centroidal axis above the bottom segment, respectively. The intersection of $M_{2,1}$ to the moment distribution gives the height of the bottom segment as 1549 mm; the top interface of the bottom segment does not open in lateral loading. The intersection of $M_{2,2}$ to the moment distribution gives the height of the bottom segment as 415 mm; the top interface of the bottom segment opens after the design drift. The moment capacity, $M_{0.004}$, indicates that the extreme fibre concrete compression strain above the bottom segment has reached 0.004. The intersection of $M_{0.004}$ to the moment distribution gives the height of the bottom segment as 292 mm. As shown in Figure 2, each test specimen was composed of four CFT segments, each of which had an outside diameter (OD) of 500 mm and a height of 500 mm plus cementitious and epoxy layers on the segment interface for leveling.

Specimen 2, as shown in Figure 2(b), included external energy-dissipating devices at the base to increase not only the energy dissipation but also the moment resistance. Figure 2(c)

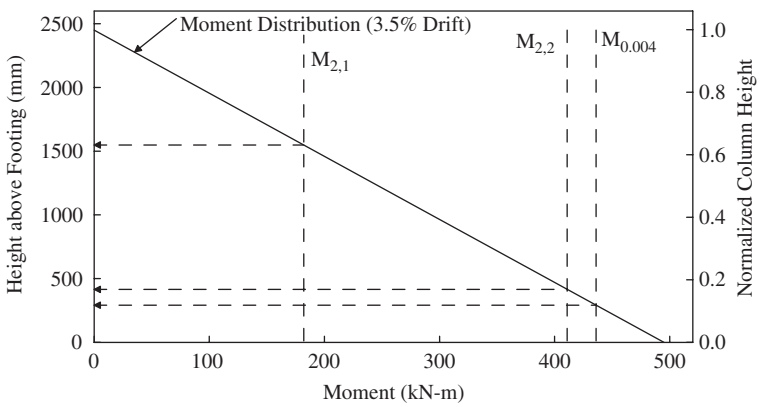

Figure 1. Moment distribution versus moment capacity at top interface of bottom segment.

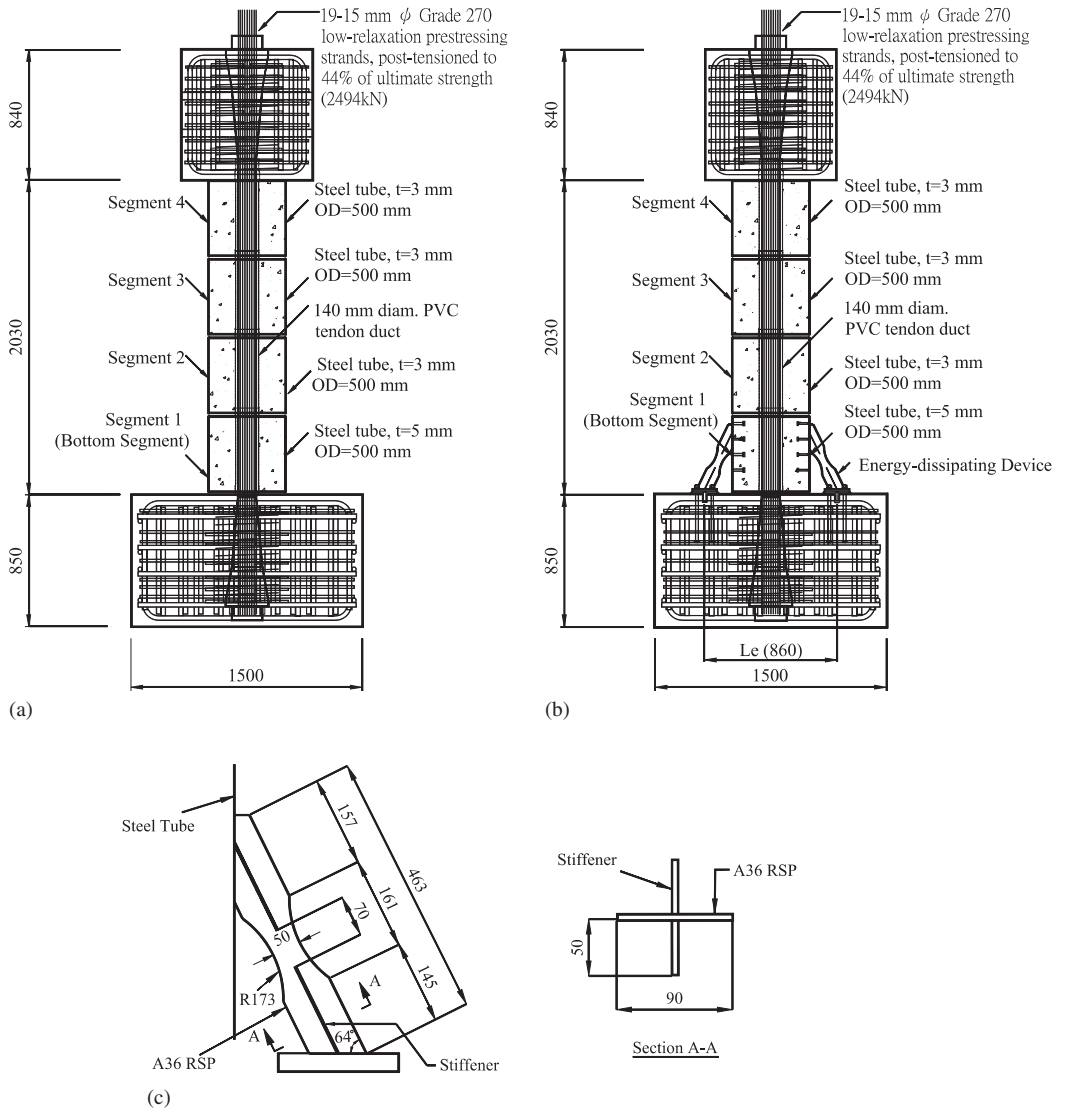

Figure 2. Specimen elevation (dimensions in millimeters): (a) Specimen 1; (b) Specimen 2; and (c) close-up of energy-dissipating device.

presents a close-up of an energy-dissipating device, which consisted of a 5-mm thick A36 Reduced Steel Plate (RSP) and stiffeners at both ends. The smallest sectional area, A_{RSP}, of the RSP was determined in order to provide 10% design moment, M_d, as follows:

$$A_{RSP} = \frac{0.1M_d}{L_e} \times \frac{1}{\sin 64^\circ} \times \frac{1}{F_y} \tag{2}$$

where F_y(= 248 MPa) is the specified yield strength of A36 steel and L_e(= 860 mm) is the distance between the two devices. Stiffeners were provided at both ends of the RSP to decrease the unbraced length so that according to AISC [10, Chapter E], the buckling strength was calculated to be $0.97F_y$ with the effective length factor of 0.5. Shear studs were placed inside the tube to transfer force in the RSP to the concrete. No shear keys between the segment interface were provided, since the substantial axial force produced by unbonded strands created a greater friction force (554 kN) than applied lateral force (194 kN). The friction coefficient was assumed to be 0.2 in computing the friction force.

EXPERIMENTAL PROGRAM

Construction and test procedure

First, the PVC pipe for the tendon duct was positioned at the centre of each tube, and the strand anchorage was positioned at the centre of the load stub and footing reinforcement cages. Then, the column segments, load stubs, and footings were cast with concrete, cured, and delivered to the laboratory to be assembled by passing strands through the tendon duct and the anchorage (see Figure 3). The specimens were post-tensioned with a hydraulic stressing

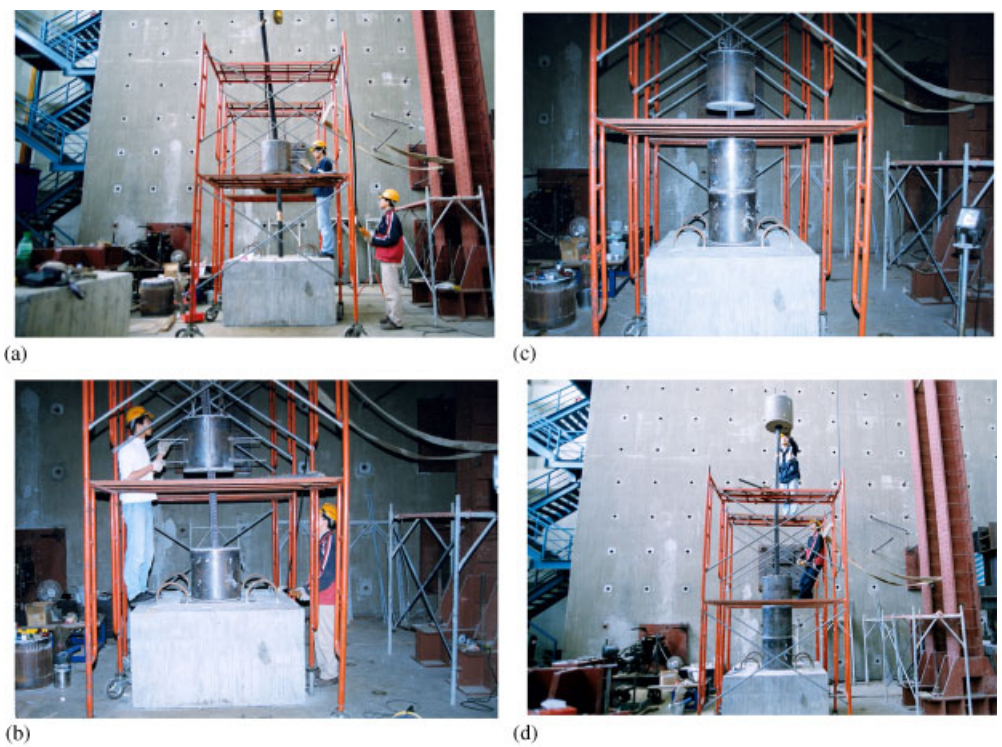

Figure 3. Specimen assembly sequence: (a) first segment; (b) second segment; (c) third segment; and (d) fourth segment.

ram, which included a pressure transducer and a calibration chart to compute the hydraulic ram load. Four strain gauges mounted on strands were connected to a data acquisition system with real-time display to monitor axial strains. The total initial post-tensioning force after losses was 2365 and 2462 kN for Specimens 1 and 2, corresponding to 95 and 99% of the design force, respectively.

A 500-kN actuator was placed at the load stub (see Figure 4), and the specimen was then tested statically with a pre-defined displacement history, consisting of one drift cycle with amplitudes of 0.1, 0.15, 0.2 and 0.3%, followed by three drift cycles with amplitudes of 0.4, 0.6, 0.9, 1.5, 2, 3, 4, 5 and 6%. The concrete compressive strengths at 28 days and on the day of testing are listed in Table I.

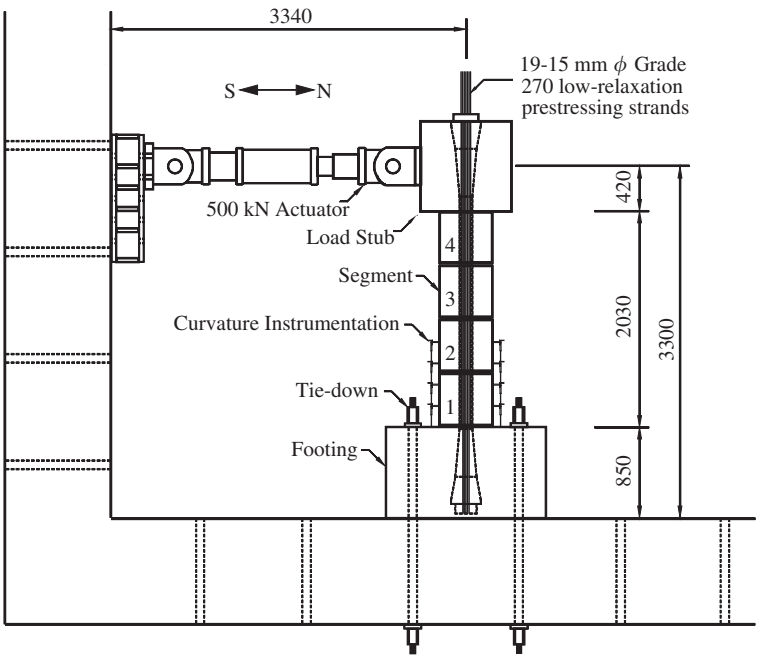

Figure 4. Test setup.

Table I. Concrete compressive strength.

Specimen no.	Design strength (MPa)	28 days (MPa)	D.O.T.* (MPa)
1	35	46	53
2	35	46	54

*D.O.T. represents day of testing.

Results of experiments

Flexural cracks of Specimen 1 at the base and the interface between segments 1 and 2 were noted before 0.6% drift, and continued to open and extend with increasing drift. The cover concrete spalled on the compression face of the base and of the interface between segments 1 and 2 at drifts of 2 and 3%, respectively. Figure 5 presents a photograph of segments 1 and 2 on the tension and compression faces at 4% drift, showing a 13-mm crack opening on the tension face at the base, larger than the 3-mm opening at the interface between segments 1 and 2. Figure 5(d) shows concrete crushing at the base, resulting in strength degradation by 4% at the maximum drift of 6% (see Figure 6(a)). The residual displacement was 10 mm, 7% of the maximum displacement, after the specimen completed a 6% drift cycle.

For Specimen 2, with the energy-dissipating devices at the base, a flexural crack at the interface between segments 1 and 2 was observed at the same drift level as for Specimen 1. A flexural crack at the base was noticed at a larger drift of 0.6%, corresponding to the buckling of an RSP in one energy-dissipating device during compression. The buckled RSP could be pulled straight into the strain hardening range in tension loading to provide energy dissipation; both RSPs fractured during the first push and pull loading cycles to 4% drift, reducing the

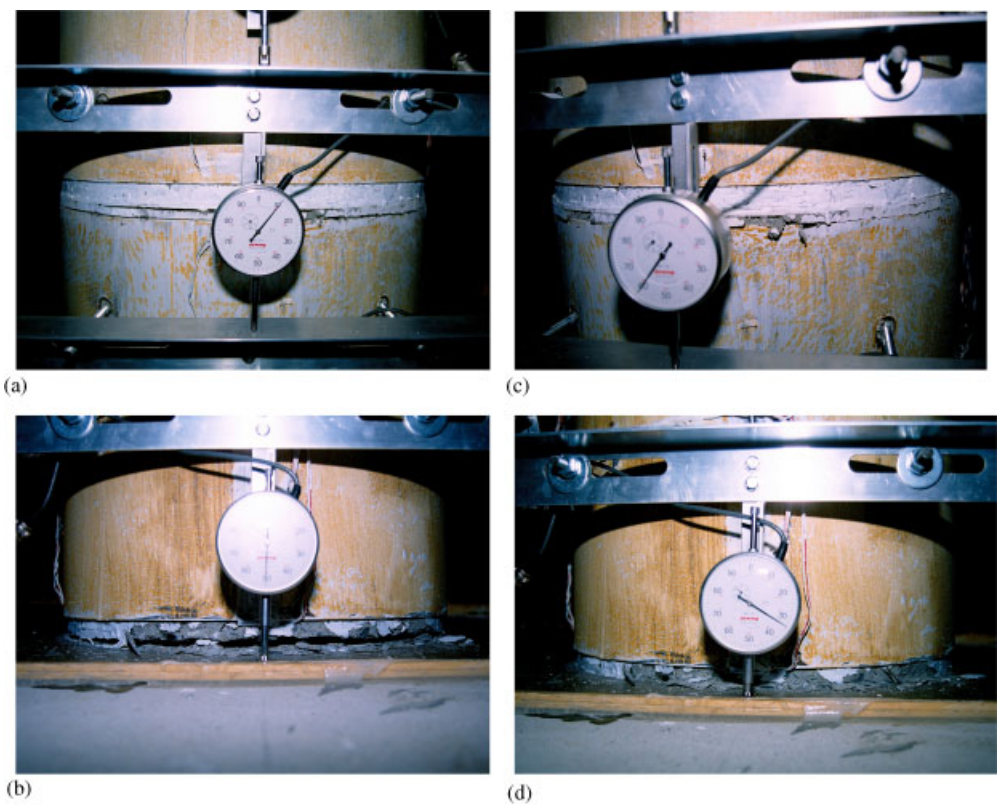

Figure 5. Specimen 1 at 4% drift: (a) opening between segments 1 and 2; (b) opening at base; (c) spalling between segments 1 and 2; and (d) crushing at base.

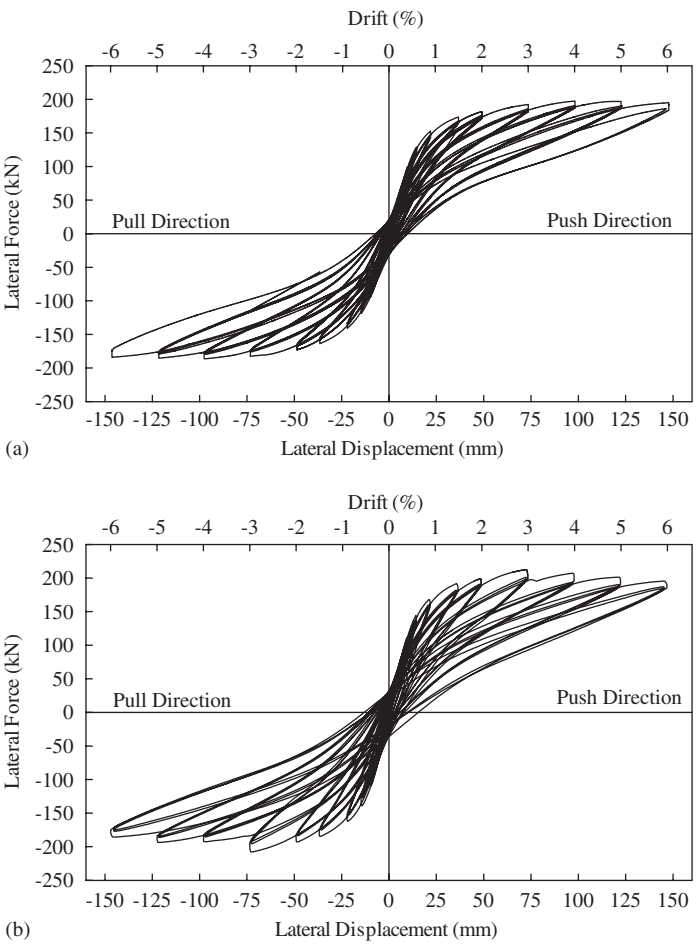

Figure 6. Lateral force versus lateral displacement response: (a) Specimen 1; and (b) Specimen 2.

flexural strength (see Figure 6(b)). Figure 7 shows a photograph of segments 1 and 2 on the tension and compression faces at 4% drift, which exhibits less opening and damage at the base than seen in Specimen 1. The test was stopped after completing three cycles of 6% drift with a residual displacement of 15 mm, 10% of the maximum displacement.

Hysteretic energy dissipation of Specimen 1 was associated with the plastic straining of concrete in compression, but that of Specimen 2 was associated with the plastic straining of an RSP in tension and of concrete in compression. Figure 8(a) shows that the hysteretic energy dissipation of Specimen 2 is about 50% higher than that of Specimen 1 before 4% drift. The percentage increase starts to decrease after fracture of the RSP, which corresponds to the variation of the equivalent viscous damping [7] as shown in Figure 8(b). Before fracture of RSPs, the computed equivalent viscous damping of Specimen 2 is 9%, higher than 6.5% of Specimen 1. The increase in equivalent viscous damping is not significant

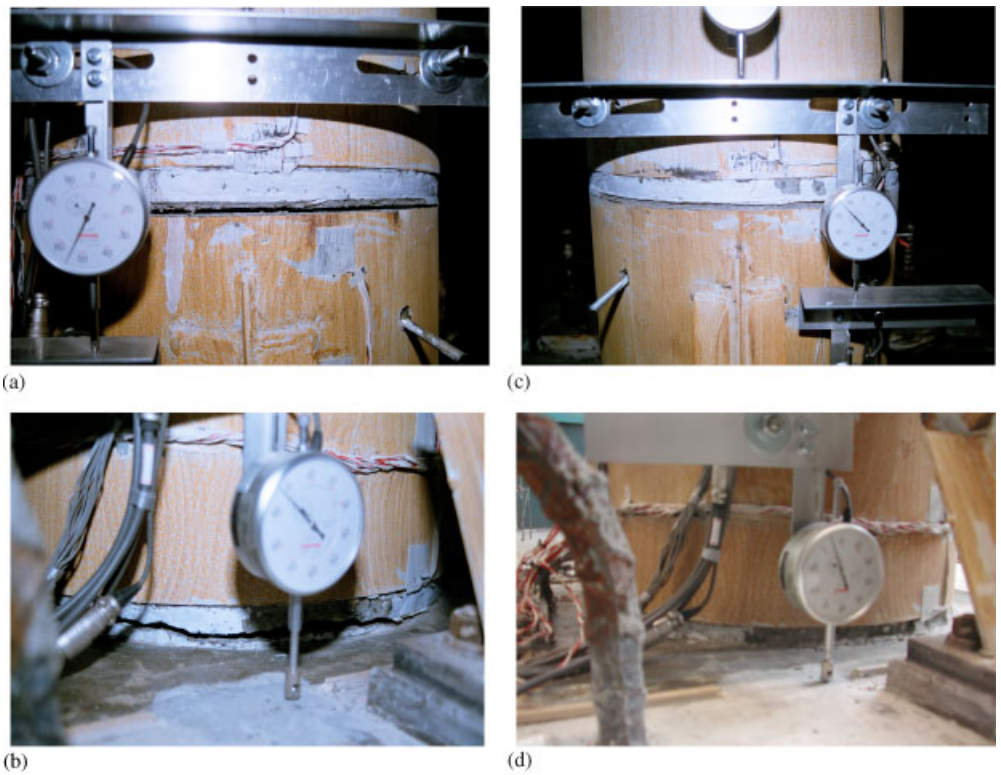

Figure 7. Specimen 2 at 4% drift: (a) opening between segments 1 and 2; (b) opening at base; (c) spalling between segments 1 and 2; and (d) crushing at base.

because it reduces the maximum displacement of a single column bent bridge by 8% based on Eurocode 8 [12]

$$\frac{\Delta_{14\%}}{\Delta_{11.5\%}} = \frac{\Delta_{5\%}[7/(2+14)]^{1/2}}{\Delta_{5\%}[7/(2+6.5)]^{1/2}} = 0.92 \tag{3}$$

where $\Delta_{14\%}$, $\Delta_{11.5\%}$, and $\Delta_{5\%}$ are the displacements for damping levels of 14, 11.5 and 5%, respectively. Note that 5% elastic viscous damping is included in Equation (3).

Strand force was computed from the strain gauge readings and the strand area. Figure 9 shows that once the gap opens, the strand force starts to increase with increasing drift, reaching 55% of the ultimate strand strength at 6% drift. A loss of the initial post-tensioning force, which was caused by concrete crushing at the base, was computed to be about 10% after the specimen completed 6% drift cycles.

Figure 10 shows the distribution of curvature along the column height for both the push and pull directions. Because the gap opening at the base exceeded measuring range of the displacement transducers after 5% drift, the curvatures at 6% drift were not obtained.

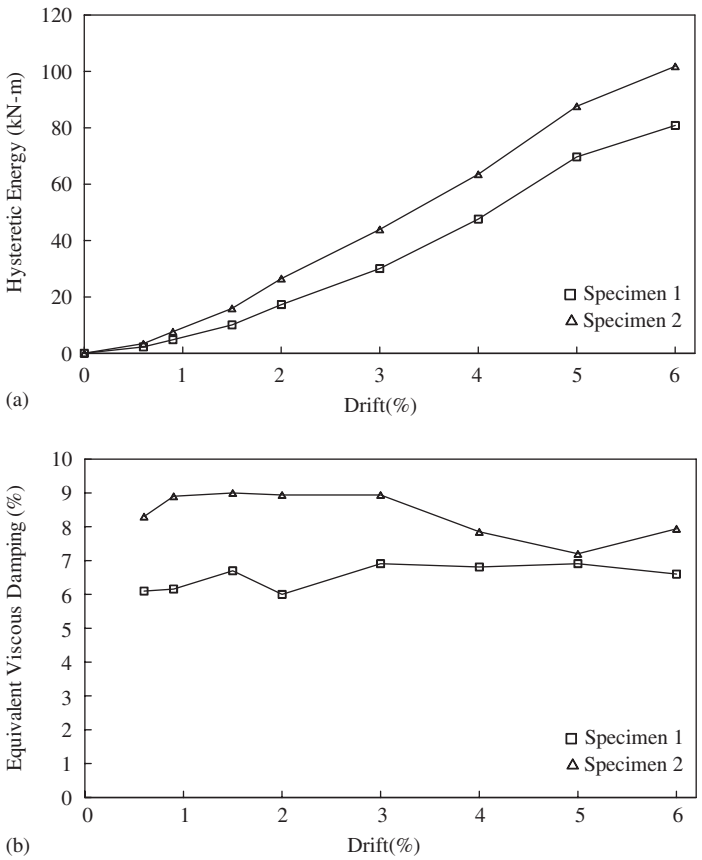

Figure 8. Hysteretic energy and equivalent viscous damping versus drift relationships: (a) hysteretic energy; and (b) equivalent viscous damping.

The experimental curvatures were calculated as

$$\phi = \frac{\Delta_t - \Delta_c}{DL} \tag{4}$$

where Δ_t is the elongation of a displacement transducer on the tension side of the segment, Δ_c is the shortening of a displacement transducer on the compression side of the segment at the same height level, D is the distance between these two displacement transducers, and L is the gauge length. The gap opening at the base is bigger than that at the interface between segments 1 and 2, leading to the curvature of Specimen 1 at the base larger than that at the interface for all drift levels (see Figure 10(a)). Additional lateral restraining to segment 1 of Specimen 2, provided by the energy-dissipating device, reduces rotation of segment 1. Thus, the curvature of Specimen 2 (see Figure 10(b)) at the base is smaller than that at the interface for a drift less than 4%. After the fracturing of RSPs, the gap opening at the interface reduces in size with increasing drift (see Figure 11), producing a smaller curvature than seen at 4% drift.

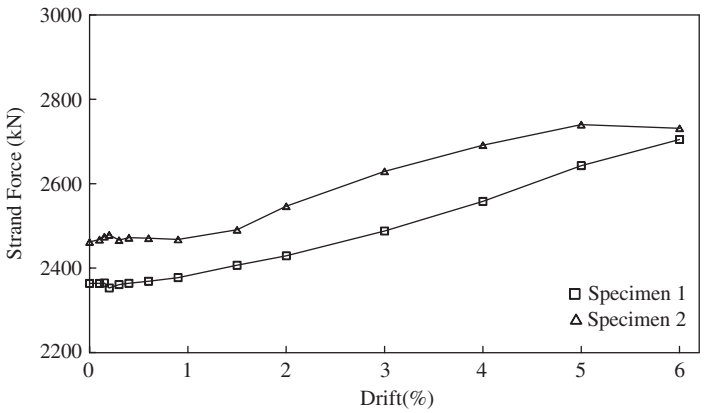

Figure 9. Strand force versus drift relationship.

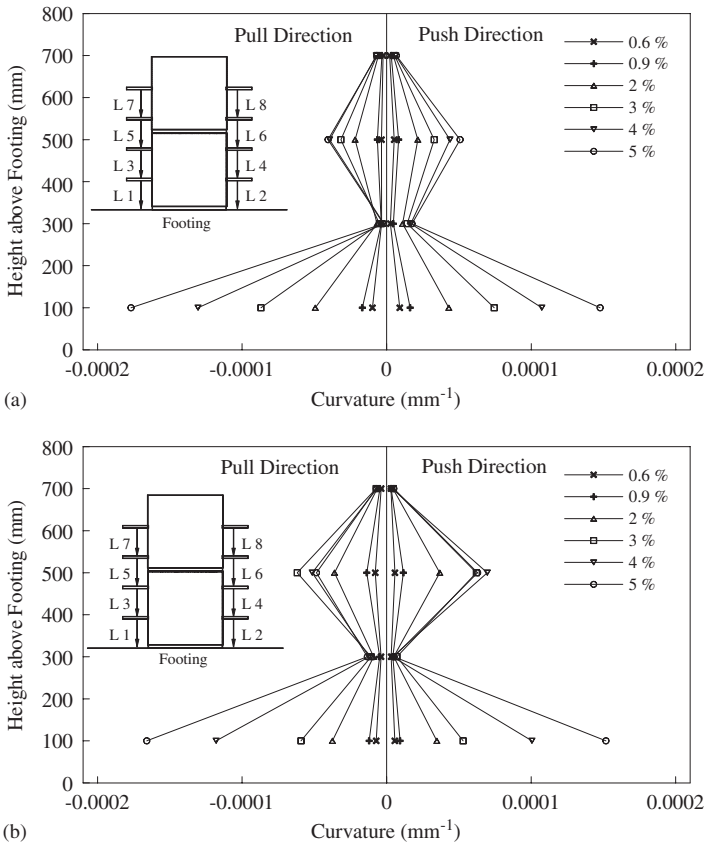

Figure 10. Curvatures along column height: (a) Specimen 1; and (b) Specimen 2.

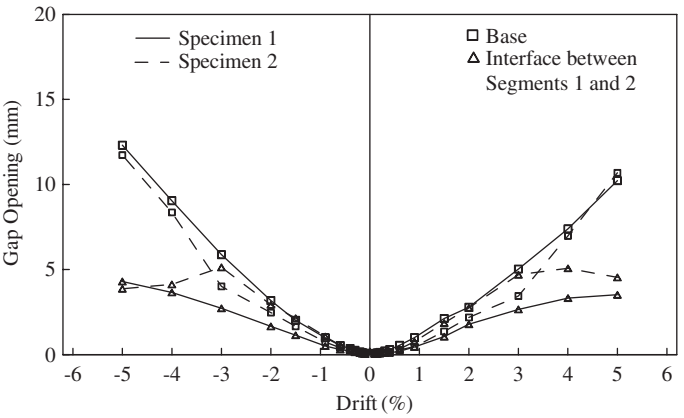

Figure 11. Gap opening versus drift relationship.

EVALUATION OF SEGMENTAL COLUMN FLEXURAL DISPLACEMENT

Hewes and Priestley [6] attributed large non-linear displacement of the segmental column to a rigid rotation of the entire column about the column base with a plastic hinge, which has a length equal to half the section diameter. This study adopted their concept to calculate the flexural displacements of each specimen with curvatures at the base, which were determined by linearly extrapolating the experimental curvatures along the segment 1 height. The computed displacements were divided by the corresponding imposed displacement to obtain the contribution as shown in Figure 12(a). Each drift has two bars; the first represents the displacement ratios of Specimen 1, and the second represents those of Specimen 2. The experimental displacement of Specimen 1 is overestimated due to a fixed plastic hinge length used for all drifts. The predicted displacement is smaller than the imposed displacement for Specimen 2, since the displacement contributed from rotation at the interface between segments 1 and 2 is not considered in this approach.

Figure 13 shows a schematic column deformation at moderate to high drifts. The column rotates not only about the base but also about the interface between segments 1 and 2; in other words, a plastic hinge is formed on each of these two locations. A method to quantify the flexural displacement caused by the two hinges is needed.

Because a clear deviation from the linear lateral force–lateral displacement response is not noted until the crack has propagated to the centroidal axis of the column (called 'first yield'), the flexural displacement, Δ_f, is estimated by

$$\Delta_f = \tfrac{1}{3}\,\phi_b H_1^2 \tag{5}$$

where ϕ_b is the curvature at the base assuming a linear distribution in the plastic hinge region in segment 1 (see Figure 14), and H_1 is the column height measured to the base. The experimental flexural displacement, Δ_f, is then expressed as

$$\Delta_f = \Delta_e + \Delta_{p1} + \Delta_{p2} \tag{6}$$

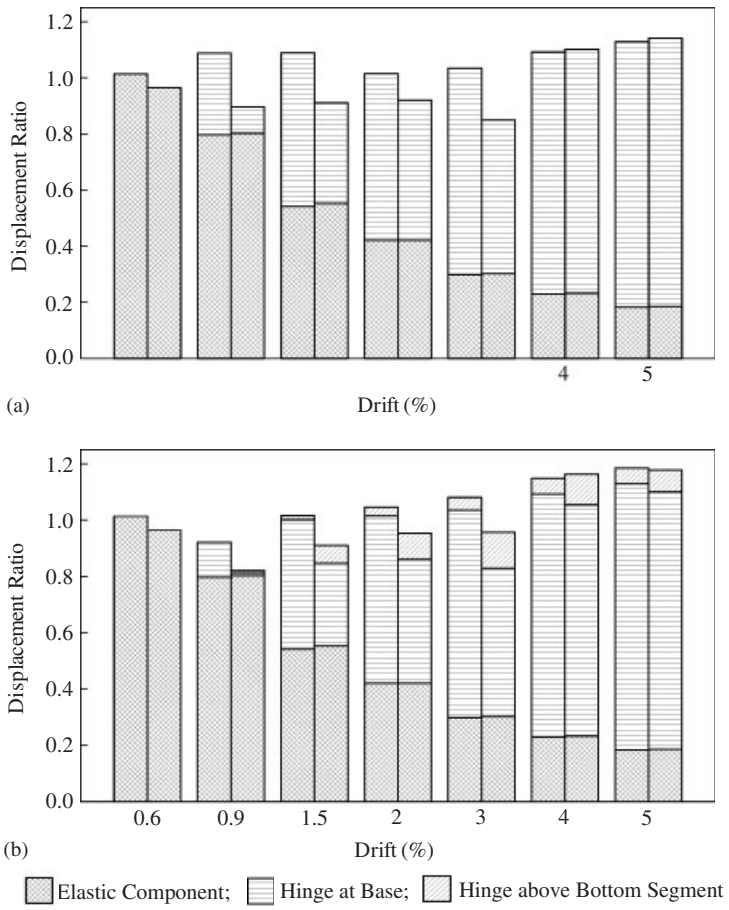

Figure 12. Distribution of lateral displacement component: (a) one plastic hinge; and (b) two plastic hinges.

where Δ_e is the elastic displacement calculated as

$$\Delta_e = \frac{1}{3}\,\phi'_{y1} \times \frac{M_1}{M'_{y1}} \times H_1^2 \tag{7}$$

where ϕ'_{y1} is the theoretical 'first yield' curvature at the base section, corresponding to the neutral axis position at the centroidal axis of the section; M'_{y1} is the theoretical 'first yield' moment at the base; and M_1 is the computed moment at the base.

The plastic displacement Δ_{p1}, resulting from rigidly rotating the entire column about the base, is expressed as

$$\Delta_{p1} = \left(\phi_b - \phi'_{y1} \times \frac{M_1}{M'_{y1}}\right) \times L_{p1} \times H_1 \tag{8}$$

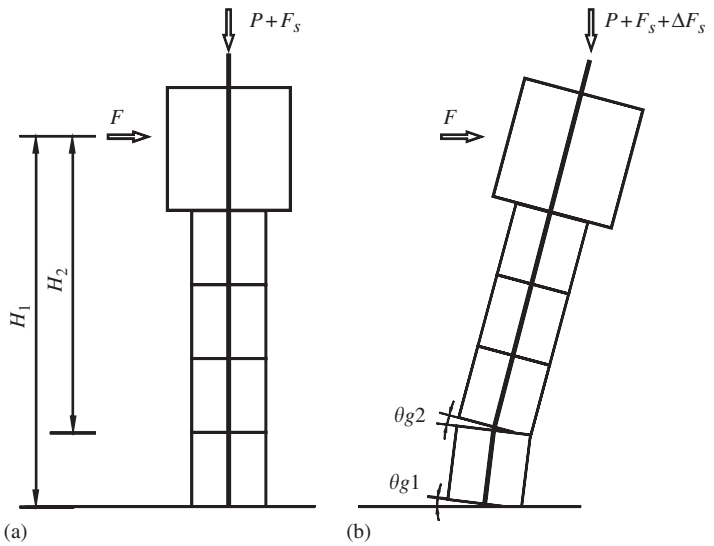

Figure 13. Schematic column deformation: (a) elastic stage; and (b) inelastic stage.

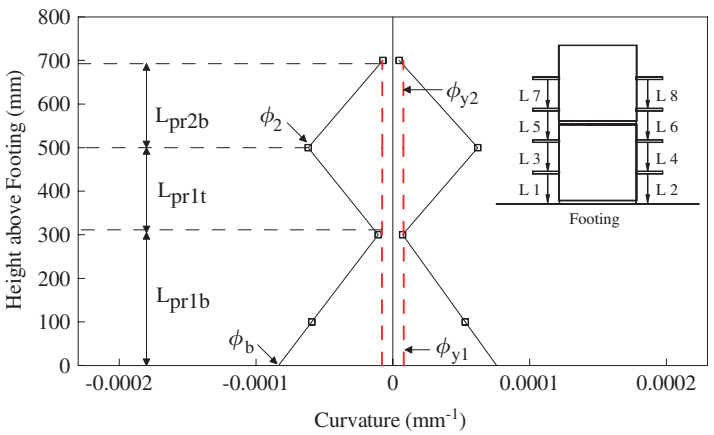

Figure 14. Plastic hinge region in segments 1 and 2.

where L_{p1} is the plastic hinge length in segment 1. The column above segment 1 further rotates about the interface between segments 1 and 2, resulting in an additional plastic displacement Δ_{p2}

$$\Delta_{p2} = \left(\phi_2 - \phi'_{y2} \times \frac{M_2}{M'_{y2}} \right) \times L_{p2} \times H_2 \tag{9}$$

where ϕ_2 is the experimental curvature at the interface between segments 1 and 2, calculated from measurements made by a pair of the displacement transducers L_5 and L_6 (see Figure 14); ϕ'_{y2} is the theoretical 'first yield' curvature at the interface, corresponding to the neutral axis

position at the centroidal axis of the section; M'_{y2} is the theoretical 'first yield' moment at the interface; M_2 is the computed moment at the interface; H_2 is the column height measured to the interface, and L_{p2} is the plastic hinge length in segment 2.

Two unknowns, the plastic hinge lengths L_{p1} and L_{p2} in Equations (8) and (9), remain to be determined to calculate the plastic flexural displacements Δ_{p1} and Δ_{p2}. Hines *et al.* [13] have shown that a plastic hinge's length is approximately half the plastic hinge region, which is defined as the region where the experimental curvature is larger than the ideal yield curvature. As shown in Figure 14, L_{pr1b} and L_{pr1t} are the plastic hinge region in the bottom and top parts of segment 1, and L_{pr2b} is the plastic hinge region in the bottom part of segment 2. The ideal yield curvatures for segments 1 and 2 are identified as ϕ_{y1} and ϕ_{y2}, respectively. Relationships of the plastic hinge region versus drift are shown in Figure 15, in which the plastic hinge region stabilizes after a drift of 2% for two segments. The plastic hinge lengths L_{p1} and L_{p2} for segments 1 and 2, respectively, are calculated as

$$L_{p1} = \tfrac{1}{2}\,(L_{pr1b} + L_{pr1t}) \tag{10}$$

$$L_{p2} = \tfrac{1}{2}\,(L_{pr2b}) \tag{11}$$

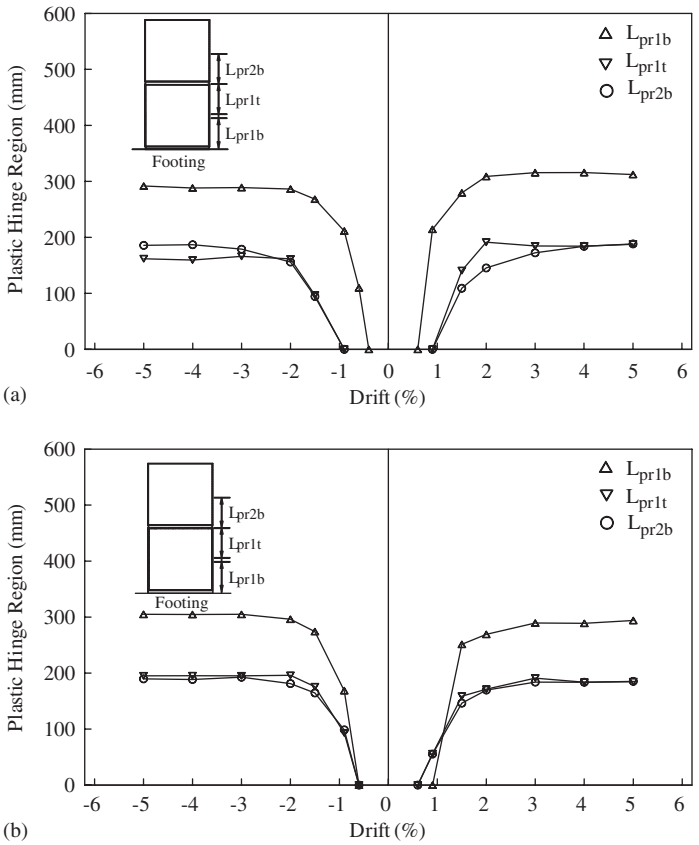

Figure 15. Plastic hinge region versus drift relationships: (a) Specimen 1; and (b) Specimen 2.

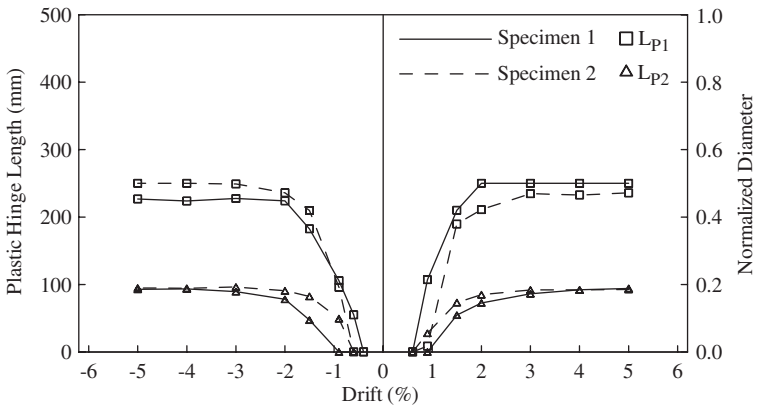

Figure 16. Plastic hinge length versus drift relationships.

The plastic hinge length increases with drift and approximates to half the section diameter in segment 1 and one-fifth the section diameter in segment 2 (see Figure 16).

Figure 12(b) shows the ratio of the computed flexural displacement Δ_e, Δ_{p1}, and Δ_{p2} to the imposed displacement at selected drifts. The flexural displacement caused by the plastic hinge above the bottom segment increases with drift and is more significant in Specimen 2 than in Specimen 1, since the energy-dissipating devices in Specimen 2 reduces rotation of the bottom segment.

CONCLUSIONS

To avoid cast-in-place concrete construction and reduce the residual displacement of the column, two ungrouted post-tensioned, precast CFT segmental bridge columns were tested under cyclic loading to evaluate the seismic behaviour of the column details. Energy-dissipating devices were placed at a specimen's base (Figure 2) to increase the energy dissipation of the hysteretic response in the unbonded post-tensioned system. The authors have only investigated the behaviour of the two specimens with a fixed axial force ratio, post-tensioned strand force, and number of segments so that the following conclusions are drawn for the study:

(1) All the precast concrete segments were encased in the steel tube, minimizing concrete spalling above the bottom segment and concrete crushing at the base at the design drift of 3.5%. Both specimens could develop the maximum flexural strength about the design drift and reach 6% drift with small strength degradation and residual displacement (Figure 6). No fracturing of strands or tube was noted.
(2) The hysteretic energy dissipation per cycle was converted to its equivalent viscous damping, which was 6.5% for Specimen 1 but was 9% for Specimen 2 due to the proposed energy-dissipating device.
(3) The column rotated not only about the base but also about the interface between segments 1 and 2, resulting in large curvatures concentrated at these two locations (Figure 10). A plastic hinge region, defined in a region where curvatures were larger

than the ideal yield curvature (Figure 14), allowed for the calculation of the plastic hinge length in the segments (Figure 16). The figure shows that Specimen 2 had a shorter plastic hinge length in segment 1 but a longer plastic hinge length in segment 2 than seen in Specimen 1 because the energy-dissipating devices provided lateral restraining to segment 1 of Specimen 2, resulting in less rotation of segment 1. After the energy-dissipating devices fractured, the plastic hinge lengths for these two specimens were close: approximately 0.5 times the section diameter in segment 1 and 0.2 times that in segment 2.

(4) A method to evaluate the experimental flexural displacement of the segmental column was developed using two instead of one plastic hinge in the column. Although the majority of plastic flexural displacement was contributed by the plastic hinge at the base, for Specimen 2 stiffened at the base the effect of second plastic hinge above the bottom segment needed to be included to predict the flexural displacement of the column (Figure 12).

ACKNOWLEDGEMENTS

The support of this research project from the Continental Engineering Corporation and Dywidag Systems International in Taiwan is greatly appreciated. The writers express their gratitude to Prof. K. C. Tsai and Dr J. T. Hewes for providing technical advices throughout this program.

REFERENCES

1. Usami T, Ge H. Ductility of concrete-filled steel box columns under cyclic loading. *Journal of Structural Engineering* (ASCE) 1994; **120**(7):2021–2040.
2. Boyd PF, Cofer WF, McLean DI. Seismic performance of steel-encased concrete column under flexural loading. *ACI Structural Journal* 1995; **92**:355–364.
3. Elremaily A, Azizinamini A. Behavior and strength of circular concrete-filled tube columns. *Journal of Constructional Steel Research* 2002; **58**:1567–1591.
4. Susantha KAS, Ge H, Usami T. Cyclic analysis and capacity prediction of concrete steel box columns. *Earthquake Engineering and Structural Dynamics* 2002; **31**:195–216.
5. Billington SL, Barnes RW, Breen JE. A precast segmental substructure system for standard bridges. *PCI Journal* 1999; **44**(4):56–73.
6. Hewes JT, Priestley MJN. Seismic design and performance of precast concrete segmental bridge columns. *Report No. SSRP 2001/25*, University of California San Diego, La Jolla, CA, 2002.
7. Priestley MJN, Seible F, Calvi GM. *Seismic Design and Retrofit of Bridges*. Wiley: New York, 1996.
8. ATC 32. Improved seismic design criteria for California bridges: provisional recommendations. *Report No. ATC-32*, Applied Technology Council, Redwood City, CA, 1996.
9. Chen Y-H. Seismic behaviour of precast concrete-filled steel tube segmental bridge column. *Master Thesis*, National Chiao Tung University, Hsinchu, Taiwan, 2004.
10. AISC. *Load and Resistance Factor Design Specification for Structural Steel Buildings*. American Institute of Steel Construction: Chicago, IL, 2002.
11. Mander JB, Priestley MJN, Park P. Theoretical stress–strain model for reinforced concrete. *Journal of Structural Engineering* (ASCE) 1988; **114**(8):1804–1823.
12. Eurocode 8. Structures in seismic regions-design. Part 1, general and building. *Report EUR 8849 EN*, Commission of the European Communities, 1988.
13. Hines EM, Seible F. Flexural deformations in reinforced concrete bridge piers. *Report No. SSRP 2001/08*, University of California, San Diego, 2001.

